Scientific Reports

https://doi.org/10.1038/s41598-026-39486-4

Article in Press

Age-dependent efficiency of magnetic drug targeting in young and old patient-specific aortic models

Received: 27 September 2025

Accepted: 5 February 2026

Published online: 09 February 2026

Cite this article as: Hosseini S.B., Almosawy W., Takrami R.K. *et al.* Age-dependent efficiency of magnetic drug targeting in young and old patient-specific aortic models. *Sci Rep* (2026). https://doi.org/10.1038/s41598-026-39486-4

Seyed Behzad Hosseini, Wala Almosawy, Rasoul Karimi Takrami, Negar Abdi & Saman Aminian

Age-Dependent Efficiency of Magnetic Drug Targeting in Young and Old Patient-Specific Aortic Models

Seyed Behzad Hosseini[1], Wala Almosawy[2,3], Rasoul Karimi Takrami[4], Negar Abdi[5], Saman Aminian[6*]

[1] Department of Engineering, University of Florence, Florence, Italy

[2] Biomedical Engineering Department, College of Engineering, University of Warith Al-Anbiyaa, Karbala, Iraq

[3] Department of Chemistry, College of Science, University of Kerbala, Karbala, Iraq

[4] Department of Mechanical Engineering, La.C., Islamic Azad University, Lahijan, Iran.

[5] Department of Radiology, Kurdistan University of Medical Sciences, Kurdistan, Sanandaj, Iran

[6] Department of Mechanical Engineering, University of Kurdistan, Sanandaj, Iran

Abstract

Magnetic drug targeting (MDT) offers a non-invasive and localized approach for improving therapeutic delivery in vascular diseases, but its efficiency is strongly affected by age-related hemodynamic changes. In this study, a computational framework was employed to compare MDT performance in young and old patient-specific aortic models reconstructed from clinical imaging. Blood was modeled using non-Newtonian Carreau, Power-law, and Casson-Papanastasiou rheologies, while nanoparticle motion was simulated

[*] Corresponding author: S.Aminian
Email: S.Aminian@uok.ac.ir

under external magnetic fields ranging from 0.5 to 1.5 T. Across all rheological models, capture efficiency (CE) increased with particle size and magnetic field intensity. Importantly, older patients consistently exhibited slightly higher CE than younger patients, a trend driven by their reduced flow velocity, enlarged aortic lumen, and lower wall shear stress, which collectively prolonged nanoparticle residence time and reduced hydrodynamic drag opposing magnetic capture. For example, under a 1.5 T field using the Carreau model, CE reached 8.7% for 1000 nm particles in both young and old patients, but at intermediate intensities (0.5–1.25 T), older patients showed higher CE (e.g., 2.4% vs. 2.1% at 0.5 T, and 7.3% vs. 6.6% at 1.25 T). Newtonian rheology consistently over-predicted CE relative to non-Newtonian models. All applied magnetic field strengths remained within clinically acceptable safety thresholds, and field localization coincided with the target region of interest. These findings demonstrate that vascular aging enhances magnetophoretic drug capture under realistic hemodynamic conditions and underscore the need for age-aware optimization in patient-specific MDT strategies.

Keywords: Capture efficiency, Aortic tumor, Casson-Papanastasiou, CFD, nanoparticles.

1. Introduction

The aorta, as the body’s principal artery, is susceptible to a range of life-threatening diseases, particularly in elderly individuals. Among these are

aortic aneurysms, dissections, chronic inflammatory degeneration, and atherosclerosis, each contributing significantly to cardiovascular morbidity and mortality. Aortic aneurysms, whether abdominal or thoracic, involve localized dilation of the aortic wall and often remain asymptomatic until rupture, which is associated with mortality rates exceeding 80% without emergency surgical intervention [1-3]. Aortic dissections, resulting from intimal tears and blood entering the medial layer, can lead to multi-organ failure or stroke, with early mortality rates of 1–2% per hour if untreated. Chronic inflammatory degeneration and atherosclerosis involve persistent vascular inflammation, leukocyte infiltration, and degradation of extracellular matrix, creating a pro-aneurysmal and thrombogenic environment [4,5]. Globally, atherosclerosis remains a leading cause of ischemic heart disease and stroke, accounting for over 17 million deaths annually, many of which are due to complications such as plaque rupture and thrombosis [6,7].

Conventional treatment of these aortic diseases depends on disease severity and location. Surgical resection, stent graft placement, and Thoracic Endovascular Aortic Repair (TEVAR) are standard approaches for aneurysms and dissections [8]. Pharmacological therapy, including antihypertensives and statins, is used to manage atherosclerosis and delay progression. However, these treatments are not without limitations. Surgical options, though lifesaving, are invasive and particularly hazardous in elderly patients with comorbidities. Critically, the descending thoracic aorta is anatomically

close to the spinal cord, making spinal cord ischemia one of the most feared complications during aortic surgery or stent deployment—leading to paraplegia in up to 8% of TEVAR cases. Furthermore, systemic drug administration often results in poor local concentration at the disease site and significant off-target toxicity [9,10].

To overcome these challenges, MDT has emerged as a promising non-invasive strategy. MDT employs superparamagnetic nanoparticles (MNPs) loaded with therapeutic agents that are guided to specific disease sites using externally applied magnetic fields. By concentrating drugs locally, MDT reduces systemic exposure and enhances efficacy. This approach was first pioneered for solid tumors, with early clinical trials demonstrating effective localization of chemotherapeutic agents in breast, brain, and liver cancers [11]. Since then, MDT has been explored in multiple oncologic applications including glioblastoma [12], lung carcinoma [13], and prostate cancer [14]. Moreover, functional coatings such as dextran and PEG have improved MNPs' stability and biocompatibility [15].

In recent years, the efficiency of MDT has been extensively investigated by examining the effect different parameters affecting it. Furlani and Ng [16] presented an analytical model to predict trajectory and capture of nanoparticles at desired site. The model takes into account various parameters, including the properties of the magnet, the size and magnetic properties of the nanoparticles, the dimensions of the blood vessel, and blood flow velocity. It was found that the model successfully demonstrates that

carrier particles can be effectively directed to tumors several centimeters away from the magnetic source, proving the viability of this drug targeting method. Ardalan, et al. [17] numerically studied the effect of geometrical parameters on the capture efficiency of nanoparticles in a stenosed blood vessel under a magnetic field. Their findings highlight that key factors such as nanoparticle diameter, magnetic field intensity, and blood velocity significantly impact the success of magnetic drug targeting. The study also considered the non-Newtonian behavior of blood and different stenosis geometries, demonstrating their importance in particle capture. In another study, Sodagar et al. [18] used a 3D model of the aortic arch to study magnetic drug delivery under realistic blood flow conditions. Their findings show that increasing microparticle diameter and optimizing the magnetic field's orientation are key to improving particle absorption efficiency. A study by Barnsley et al. [19] used both numerical models and physical experiments to investigate how nanoparticles are captured in blood vessels. They specifically looked at vessels with and without stenosis (narrowing) while using a Halbach array of permanent magnets. The research found that several factors significantly influence nanoparticle capture, including the magnet's shape and angle, the speed of the fluid flow, and the presence of stenosis.

In their recent work, Hewlin and Tindall [20] examined the ability to capture nanoparticles within a computer-based model of the “Circle of Willis” specific to each patient. After comparing nanoparticle trajectories due to realistic

arterial curvature and pulsatile flow, they found that both properties of the arterial system greatly affected the targeting success rate of the captured particles. Also recently, Hewlin et al. [21] studied the effect of unsteady flow on the capture of nanoparticles in a stented carotid artery with a magnetic stent and found that both the pulsation and the local hemodynamic conditions had a large impact on the way that nanoparticles were captured. Together, these studies stress the need to use patient specific anatomical and physiological characteristics when determining how well the MDT will work.

In their study, Alizadeh et al. [22] numerically investigated how the injection angle of carrier nanoparticles affects their capture efficiency under the influence of various magnetic fields. The study's key findings highlighted that the injection angle is a critical parameter, and an optimal angle exists for maximizing the capture of nanoparticles. Jalali et al. [23]conducted a numerical study using pulsatile blood flow simulations to investigate MDT. The research focused on the dispersion and capture of drug particles in both symmetrically and asymmetrically stenosed blood vessels. The study's key findings reveal that the pulsatile nature of blood flow significantly influences particle movement and capture efficiency. Furthermore, the specific geometry of the stenosis, whether symmetric or asymmetric, was found to have a considerable impact on the drug particles' trajectory and deposition within the vessel. Xu et al. [13]conducted a numerical simulation to explore a non-invasive approach to magnetic drug targeting for lung cancer therapy using a bulk superconducting magnet. Their study found that this type of

powerful magnet could effectively capture magnetic drug particles even from a distance, overcoming the limitations of conventional magnets. This research suggests a promising path toward developing an external and practical system for targeted drug delivery to the lungs. Finally, In their study, Sharma et al. [24] performed a simulation of magnetic drug delivery in stenotic arteries, incorporating a more complex model of blood flow. Their research specifically considered a two-phase blood flow model and the influences of the Hall effect and ions, which are not typically included in simpler models. The findings of this study provide a more detailed understanding of magnetic drug delivery by highlighting the significant roles of two-phase blood flow, the Hall effect, and ion concentration on the effectiveness of particle deposition within stenosed vessels. Despite these developments, a major research gap remains which is that no prior study has applied MDT to real patient-specific aortic geometries in elderly individuals, who represent the most vulnerable group for aortic pathologies. Moreover, the complex interplay of aging vasculature, altered hemodynamics, and non-Newtonian blood behavior in aorta under MDT conditions has not been systematically explored in a clinically relevant setting.

Despite the growing interest in magnetic drug targeting, limited research has systematically addressed the influence of vascular aging on nanoparticle transport and capture efficiency. Many previous studies have relied on simplified or idealized geometries and single rheological assumptions, thereby neglecting the complex interplay between vascular morphology,

blood rheology, and magnetic trapping. To overcome these limitations, the present study employs real three-dimensional reconstructed aortic geometries from young and old patients together with multiple non-Newtonian blood models, including Carreau, Power-law, and Casson-Papanastasiou formulations, to capture age-related hemodynamic variations more accurately. Capture efficiency is evaluated across a range of nanoparticle diameters and magnetic field intensities, providing a comprehensive assessment of MDT performance under physiologically relevant conditions. The novelty of this study lies in its direct comparison of age groups under identical magnetic field conditions, while simultaneously integrating realistic vascular reconstructions and advanced rheological modeling, thereby isolating the effect of aging on nanoparticle capture. Ultimately, the findings establish a foundation for patient-specific optimization of MDT and emphasize the need for age-aware strategies in the clinical translation of this method.

2. Materials and methods

2.1. Geometry

To simulate drug delivery with anatomical accuracy, a patient-specific aortic geometry was reconstructed from contrast-enhanced computed tomography (CT) angiography data. The dataset, acquired in DICOM format, consisted of sequential cross-sectional images with a spatial resolution sufficient to capture detailed vascular structures. The segmentation process was carried out using Materialise Mimics v17.0 (Materialise NV, Belgium;

https://www.materialise.com), a medical image processing software designed for accurate 3D reconstruction. As shown in Fig. 1, the thoracic aorta was carefully segmented across three anatomical planes: (a) the coronal view, (b) axial slices, and (c) sagittal plane. The lumen of the aorta was manually delineated and then refined using intensity thresholding and morphological operations to isolate the vessel wall and exclude surrounding tissues. Each slice was verified to ensure continuity of the vessel and minimize segmentation artifacts. Following segmentation, the generated contours were stacked to form a 3D volumetric model of the thoracic aorta. This model was then exported in STL format and imported into 3-Matic software (Materialise) for surface smoothing and mesh optimization. The final geometry, depicted in Fig. 1(d), preserved the full anatomical curvature of the aortic arch and descending aorta, enabling realistic simulation of hemodynamic conditions. This accurate geometric representation forms the basis for the subsequent computational modeling of magnetic drug targeting.

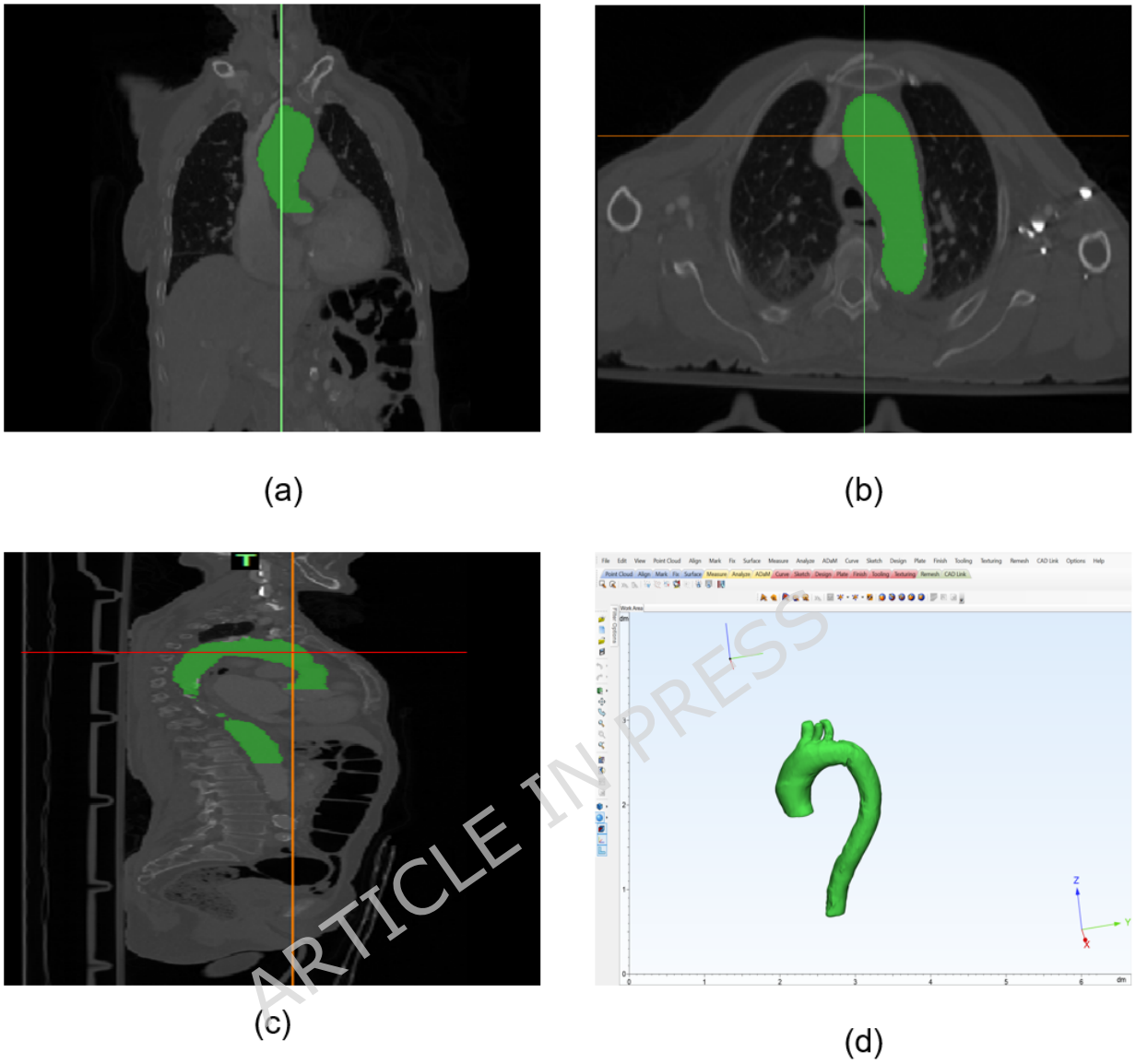

Fig. 1. CT-based reconstruction process of the patient-specific aortic geometry. (a) Coronal view of the thoracic aorta segmented in green; (b) Axial CT slice showing the lumen of the aorta; (c) Sagittal view capturing the full curvature of the aortic arch and descending aorta, (d) Final 3D reconstructed aorta rendered in 3-matic software.

The aorta of two patients (a 22-year old, and a 78-year old) have been reconstructed and used in the present study. Fig. 2 represents the aorta of

both patients. Notable differences in geometry are observed between the younger and older subjects. The aorta of the 22-year-old (Fig. 2a) exhibits a relatively slender, elongated, and smoother morphology with less curvature along the arch and descending segment. In contrast, the 78-year-old's aorta (Fig. 2b) demonstrates a more dilated structure, particularly in the ascending portion and arch. The curvature of the arch is more pronounced, and the descending thoracic aorta appears tortuous, reflecting age-related remodeling. These differences are consistent with known physiological changes in aging, such as vessel wall stiffening, dilation, and loss of elastic recoil, which collectively contribute to altered hemodynamic patterns in elderly individuals.

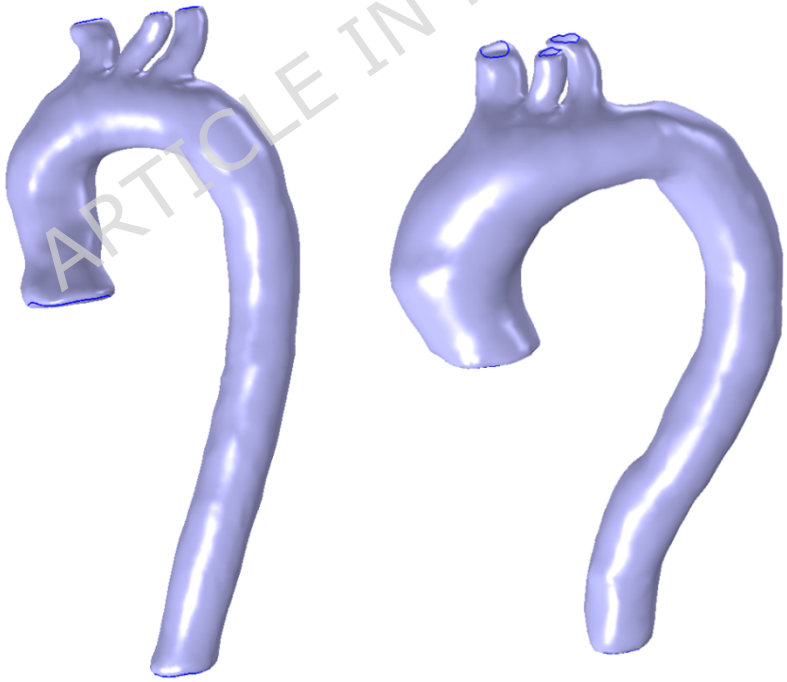

(a) (b)

Fig. 2. 3D reconstructed aorta geometry of (a) 22-year old, and (b) 78-year old woman.

Table 1 summarizes the cross-sectional areas of the anatomical regions reconstructed for the two patient-specific aortic models. As expected for two individuals of different age and anatomical background, the geometries exhibit noticeable inter-subject variability. In the ascending aorta, the younger patient model has a cross-sectional area of 530.55 mm^2, whereas the older patient model shows 962.17 mm^2. The descending thoracic aorta similarly differs between subjects, measuring 214.30 mm^2 in the younger case and 349.21 mm^2 in the older case. Variations are also present in the supra-aortic branches: for example, the brachiocephalic artery areas are 55.86 mm^2 and 118.53 mm^2, and the left common carotid artery areas are 19.38 mm^2 and 43.64 mm^2 in the younger and older models, respectively. These geometric differences represent natural inter-subject variability between the two cases and should not be interpreted as population-level age-related trends. Instead, they provide two distinct anatomical scenarios for evaluating how geometry influences magnetic particle transport. A multi-patient dataset would be required to draw statistically supported conclusions regarding geometric aging effects, which is an important direction for future work. Besides, it should be noted that all methods were performed in accordance with relevant guidelines and regulations.

Table 1. Area of different domains of both aortas.

Domain	Young patient	Old patient
Ascending Aorta	530.55 mm^2	962.17 mm^2
Descending Thoracic	214.3 mm^2	349.21 mm^2
Brachiocephalic Trunk	55.86 mm^2	118.53 mm^2
Left Common Carotid Artery	19.38 mm^2	43.64 mm^2
Left Subclavian Artery	30.41 mm^2	76.728 mm^2

To create the external magnetic field, a single axial magnetized NdFeB cylinder with diameter of 50mm and length of 100mm was used. The NdFeB magnet was assumed to be uniformly magnetized, which is the common approximation for large blocks of NdFeB magnets when modeling the external magnetic field. The dimensions chosen for this magnet are representative of high excited state energy ND-Fe-B magnets commonly used in deep target experimental arrangements and are designed so that when the Nd-Fe-B magnets are magnetized to their typical remanent flux densities, the surface magnetic flux density along the aortic wall will be in the region of 0.5-1.5 T as studied. A configuration using a Halbach array was not utilized.

2.2. Mathematical formulations

The governing equations employed in the present study are formulated to account for the three interacting phases: the blood flow (fluid phase), the external magnetic field (magnet phase), and the drug-carrying nanoparticles

(particle phase). For each phase, the corresponding equations and associated parameters are described in detail below.

2.2.1. Blood phase

In this study, the governing equations for blood flow in the patient-specific aortic geometry are based on the three-dimensional, incompressible, and non-Newtonian Navier–Stokes formulation.. The fluid is treated as incompressible and governed by the conservation of mass and momentum: Furthermore, to more accurately reflect the rheological behavior of blood flow, the governing equations are formulated in a coupled manner.

$$\nabla.\overrightarrow{u_b} = 0 \tag{1}$$

$$\rho_b\left(\frac{\partial\vec{u}_b}{\partial t} + \vec{u}_b \cdot \nabla\vec{u}_b\right) = -\nabla\vec{p} + \mu_b\nabla^2\vec{u}_b \tag{2}$$

where ρ_b, $\overrightarrow{u_b}$, $\vec{p}$ and μ_b denote the density, velocity, pressure and viscosity of blood, respectively. In the present study, three different non-Newtonian models are used to capture the non-Newtonian behavior of blood.

2.2.1.1. Power-law

To capture the shear-thinning behavior of blood, especially under varying flow conditions in large arteries, the Power-law model is employed as one of the non-Newtonian viscosity formulations. This model assumes that the apparent viscosity of blood depends solely on the local shear rate, and it effectively characterizes the reduction in viscosity with increasing shear rate,

a hallmark of non-Newtonian fluids such as blood. The effective dynamic viscosity in the Power-law model is defined by the relation [25]:

$$\mu_{eff} = K(\dot{\gamma})^{n-1} \quad (3)$$

where K is the flow consistency index (Pa.s^n), $n = 0.7755$ is the flow behavior index, and $\dot{\gamma}$ is the shear rate (s^{-1}).

2.2.1.2. Carreau Model

To capture the shear-thinning characteristics of blood with improved accuracy across a broad range of shear rates, the Carreau model is adopted as one of the non-Newtonian viscosity models in this study. This model has been widely used in hemodynamic simulations due to its smooth and continuous transition between low and high shear rate regimes, making it suitable for complex vascular geometries. The apparent dynamic viscosity μ_{eff} of blood in the Carreau formulation is defined as [26]:

$$\mu_{eff} = \eta(\dot{\gamma}) = \eta_\infty + (\eta_0 - \eta_\infty)[1 + (\lambda\dot{\gamma})^a]^{\frac{n-1}{a}} \quad (4)$$

where $n = 0.2128$, $a = 0.64$, and $\lambda = 8.2s$ denote the power-law index, dimensionless fitting parameter, and time constant, respectively. Besides, η_0 is is the zero-shear viscosity, and η_∞ is the infinite-shear viscosity [27]. The Carreau–Yasuda model offers a key advantage over simpler models like the Casson model due to its continuity at all shear rates ($\dot{\gamma} \geq 0$). For shear-thinning fluids such as blood, where n<1, the model behaves asymptotically:

as $\dot{\gamma}\to 0$, $\mu_{eff}\to\eta_0$, and as $\dot{\gamma}\to\infty$, $\mu_{eff}\to\eta_\infty$. This enables the model to capture Newtonian behavior at extreme shear conditions, while accurately reflecting non-Newtonian characteristics in the intermediate range.

2.2.1.3. Casson–Papanastasiou Model

The Casson–Papanastasiou model is used to represent the yield-stress behavior of blood, particularly in low-shear regions. Unlike the standard Casson model, which becomes discontinuous at zero shear rate, the Papanastasiou regularization introduces a smoothing function to ensure numerical stability [28]:

$$\mu_a = \left[\left(f_p\sqrt{\frac{\tau_0}{\dot{\gamma}}} + \sqrt{K}\right)^2\right] \; with \; f_p = 1 - \exp\left(-m_p\dot{\gamma}\right) \tag{5}$$

where τ_0= 0.01082 Pa is the yield stress, $K=3.1\times10^{-3}$ Pa.s is the consistency index, f_p is and m_p>100 is Papanastasiou regularization parameter [29].

2.2.2. Magnetic field phase

In this study, the magnetic field is generated using a cylindrical permanent magnet. The magnet is axially magnetized along the z-axis and positioned near the aortic wall to attract superparamagnetic drug carriers. Magnetic flux density is calculated using following equation:

$$\nabla.\vec{B} = 0 \tag{6}$$

$$\nabla \times \vec{H} = 0 \tag{7}$$

$$\vec{B} = \mu_0(\vec{M} + \vec{H}) \tag{8}$$

where $\vec{B}$, is the magnetic flux density (T), $\vec{H}$ is the magnetic field intensity (A/m), and $\vec{M}$ is the magnetization vector (A/m). The constant $\mu_0 = 4\pi \times 10^{-7}$ H/m denotes the permeability of free space. The magnetic scalar potential φm is used to compute the magnetostatic field in regions outside the magnet, such that $\vec{H} = -\nabla\varphi m$. A zero-scalar-potential boundary (V_m) was applied on the outer computational boundary to close the magnetostatic problem.

2.2.3. Particle phase

Newton's second law is employed to monitor the movement of carrier nanoparticles in the aorta. [30].

$$\sum \vec{F} = \frac{d(m_p \overrightarrow{u_p})}{dt} \tag{9}$$

where $\overrightarrow{u_p}$ and $\vec{F}$ represent the particle speed and force acts on carrier particles. The left-hand side represents the sum of forces acting on nanocarriers, while right-hand term denotes the particles' acceleration resulting from these forces. Particle mass, m_p, is calculated by following formula:

$$m_p = \frac{1}{6}\pi d_p^3 \rho_p \tag{10}$$

The most significant forces applied to nanocarriers include drag, magnetic, and Buoyancy. There are several forces acting on the carrier nanoparticles within the blood flow. In this paper, drag, magnetic, and Buoyancy forces are the considered. Particle–particle interactions and Brownian diffusion were neglected, as the nanoparticle suspension was sufficiently dilute and the particle sizes (250–1000 nm) render Brownian displacement negligible compared with convective and magnetophoretic transport. Therefore, the Eq. (6) is given as below:

$$\vec{F}_D + \vec{F}_M + \vec{F}_B = \frac{d(m_p \overrightarrow{u_p})}{dt} \tag{11}$$

The applied drag force on the carrier nanoparticle by blood is expressed by equation based on schiller-Naumann model [31]:

$$F_D = \frac{18 \cdot \mu}{\rho_p d_p^2} \cdot \frac{C_D \cdot Re_p}{24} \cdot m_p \cdot (U - u_p) \tag{12}$$

where , C_D represents the drag coefficient. This parameter for spherical particles is expressed as below [32]:

$$C_D = \frac{24}{Re_p}\left(1 + 0.15 Re_p^{0.687}\right) \tag{13}$$

The Reynolds number of nanoparticles defined by following equation:

$$Re_p = \frac{\rho|\overrightarrow{u_b} - \overrightarrow{u_p}|d_p}{\mu} \tag{14}$$

Magnetic force applied to the particles moving within the blood artery is expressed as below:

$$\vec{F}_M = \mu_0 V_p \chi (\vec{H} \cdot \nabla)\vec{H} \tag{15}$$

where , $\mu_0 = 4\pi \times 10^{-7} NA^{-2}$ represents the permeability of magnet in vacuum. In addition, V_p, and χ denote volume of nanoparticles, and magnetic susceptibility of the particle, respectively. The magnetization of these particles is presumed to be roughly proportional to applied magnetic field. Beyond a specific magnetic field value, the magnetization reaches saturation, stabilizing at a constant value Msat , given by:

$$\vec{F}_M = \mu_0 V_p \chi (\vec{H} \cdot \nabla)\vec{H} \tag{16}$$

where $\mu_0 = 4\pi \times 10^{-7} NA^{-2}$ is the permeability of magnet in vacuum. Magnetization of a matter can be calculated as below [30]:

$$\vec{M} = \begin{cases} \chi_{eff} \vec{H} & H < M_{sat}/\chi_{eff} \\ M_{sat} \dfrac{\vec{H}}{} & H \geq M_{sat}/\chi_{eff} \end{cases} \tag{17}$$

where $X_{eff} = {}^{3X_i}\!/_{(3+X_i)}$ represents the magnetic susceptibility of a spherical particle. By substituting Eq. (19) into Eq. (20), the final form of magnetic force equation is obtained.

$$\overrightarrow{F_M} = \begin{cases} \dfrac{\pi d_p^3}{6} \mu_0 \dfrac{\chi_{eff}}{2} \nabla \vec{H}^2 & H < M_{sat}/\chi_{eff} \\ \dfrac{\pi d_p^3}{6} \mu_0 M_{sat} \nabla H & H \geq M_{sat}/\chi_{eff} \end{cases} \tag{18}$$

The buoyancy force acting on a particle immersed in a flowing fluid is given by:

$$F_B = m_p \left(1 - \frac{\rho_f}{\rho_p}\right) g \tag{19}$$

where ρ_f, and ρ_p are particle fluid density, and particle density, respectively.

By substituting the forces into Eq. (12) we have:

$$\frac{d\left(m_p \vec{u}_p\right)}{dt} = \underbrace{\frac{1}{2} C_D \rho_f A_p \left|\vec{u}_f - \vec{u}_p\right| \left(\vec{u}_f - \vec{u}_p\right)}_{Drag} + \underbrace{\mu_0 V_p \chi (\vec{H} \cdot \nabla)\vec{H}}_{Magnetic} - \underbrace{V_p (\rho_p - \rho_f)\vec{g}}_{Buoyancy} \tag{20}$$

By simplifying the final equation is obtained:

$$\frac{d\left(m_p \vec{u}_p\right)}{dt} = \frac{1}{2} C_D \rho_f \left(\frac{\pi d_p^2}{4}\right) \left|\vec{u}_f - \vec{u}_p\right| \left(\vec{u}_f - \vec{u}_p\right) + \mu_0 \left(\frac{4}{3}\pi\left(\frac{d_p}{2}\right)^3\right) \chi(\vec{H} \cdot \nabla)\vec{H} - \left(\frac{4}{3}\pi\left(\frac{d_p}{2}\right)^3\right)(\rho_p - \rho_f)\vec{g} \tag{21}$$

The CE is defined as below to evaluate the efficiency of the MDT:

$$CE = \frac{N_{captured}}{N_{injected}} \tag{22}$$

where and represent the number of captured particles at ROI, and total number of released particles.

3. Results

The numerical simulation was performed using COMSOL Multiphysics v6.2 (COMSOL AB, Sweden; https://www.comsol.com) to evaluate the efficiency of MDT within a patient-specific aortic geometry reconstructed from CT angiography. A multiphysics approach was employed, combining fluid dynamics, magnetostatics, and particle tracing in a time-dependent framework. The fluid domain was governed by the incompressible Navier–Stokes equations, solved using the PARDISO solver. The magnetic field generated by an axially magnetized cylindrical permanent magnet (50 mm radius, 100 mm height) was computed using the GMRES iterative solver, while particle trajectories were tracked via Newton's second law using the FGMRES solver.

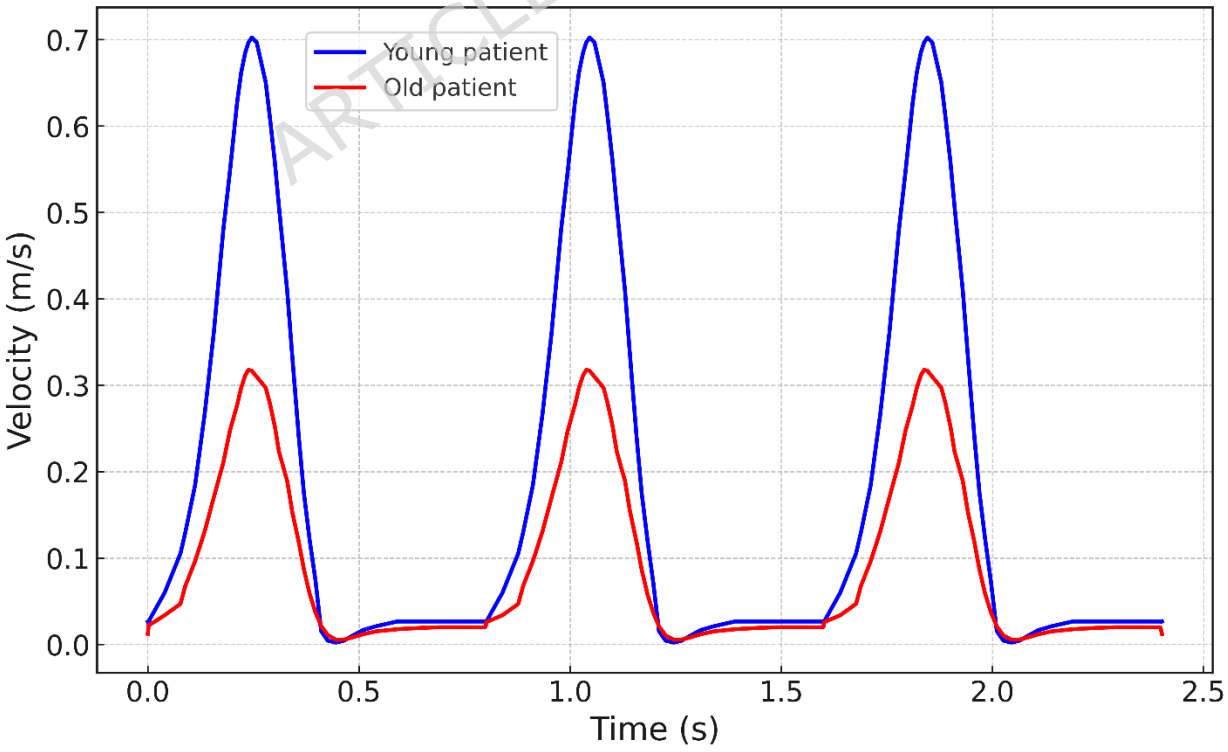

Fig. 3. Inlet velocity profiles for yound and old patients.

Blood was modeled as an incompressible, non-Newtonian fluid with a density of 1060 kg/m³. Dynamic viscosity was defined by one of three non-Newtonian models (Power-law, Carreau–Yasuda, or Casson–Papanastasiou), implemented via a user-defined function. Four diameters of magnetic nanoparticles, i.e., 250nm, 500nm, 750nm, and 1000nm, and density of 5000 kg/m³ were used. Total number of 3000 nanoparticles were released at t = 0 s at the aortic inlet, with initial velocities matching the local inlet flow and time-dependent injection was not considered. Boundary conditions were defined based on physiological relevance. In order to accurately simulate the realistic aortic inflow into the ascending aorta, a pulsatile velocity waveform based on a physiological waveform was assigned to the inlet of the ascending aorta (Fig. 3). A physiological pulsatile velocity waveform was selected from previously published Doppler ultrasound data obtained from 20 healthy adults [33]. The profile of the waveform remained consistent among all subjects, but the peak velocity of each waveform was adjusted to account for age-dependent cardiac output and size of the inlet aorta diameter. The peak systolic velocities for the young and old patients were 0.70 m/s and 0.32 m/s, respectively. The pulsatile inlet velocity waveform had a cardiac period of 0.8 s (heart rate ≈ 75 beats/min). Three cardiac cycles were simulated, and data from the third cycle were used for analysis to ensure that transient effects related to initial conditions had dissipated. At the outlet boundaries, a zero-gauge-pressure condition was imposed independently at each terminal

branch, including the brachiocephalic artery, left common carotid artery, left subclavian artery, and descending thoracic aorta. Zero-gauge-pressure boundary velocities were used to place boundaries on the outflow; this is the procedure that has been used for many years in velocity-driven CFD studies. Therefore, the computed pressures will provide relative (gauge) pressures at the outlet plane and will not indicate actual physiological pressures (90-120 mmHg). Since the ability of a nanoparticle to be captured is based more on how the fluid moves through the body than on an actual valvular blood pressure, this type of formulation will maintain the correct hemodynamics for an MDT investigation. To reproduce similar pressures in a Windkessel or RCR approach would be a future test or extension of this work. No-slip conditions were used for vessel walls. In this study, it is assumed that when particles come into contact with a blood vessel, they become permanently attached. This condition is referred to as a "freeze-upon-contact" model, and it is the standard method used to estimate the theoretical maximum capture efficiency when running MDT simulations. We do not consider any other effects that occur after the initial contact, such as gravitational settling, Saffman lift, Brownian diffusion, or partial detachment, because the effects of these forces are negligible relative to the forces from magnets and hydrodynamics acting on 250-1,000 nm particles. Therefore the capture efficiency values listed in our data should be viewed as theoretical maxima, as the actual amount of adhesion will be lower than what was calculated due to the impact of other physical and chemical interactions that have not been

accounted for in this study.Two distance from the center of magnet to the center of vessel (Lm) of 4cm and 5cm were used for the simulation. The distances are chosen because they at that distances the magnet is at outside of the body with the minimum distances from the aorta.

3.1. Validation of results

Validation of results have been performed by reproducing the results reported in the recently pubslished work by Aminian, et al. [27]. To this end, the same geometry, boundary conditions, and parameters were used. Fig. 4 illustrates the comparison between the two datasets for nanoparticle diameters of 250 nm, 500 nm, 750 nm, and 1000 nm over the third cardiac cycle. The results of the present study (blue bars) demonstrate an excellent agreement with the experimental reference (red bars), with deviations of less than 1.5% across all particle sizes.

At dp = 250 nm, the capture efficiency was 23.91% in the present study compared to 23.50% in Aminian, et al. [27], indicating a negligible difference of 0.41%. Similarly, for dp = 500 nm, the predicted CE was 35.48%, while the experimental data reported 34.10%, with a difference of 1.38%. For dp = 750 nm, the difference narrowed to 0.22% (47.12% vs. 46.90%), confirming high consistency between both studies. Finally, at dp = 1000 nm, the present model predicted 55.60%, compared to 54.10% reported experimentally, corresponding to the maximum difference observed (1.50%).

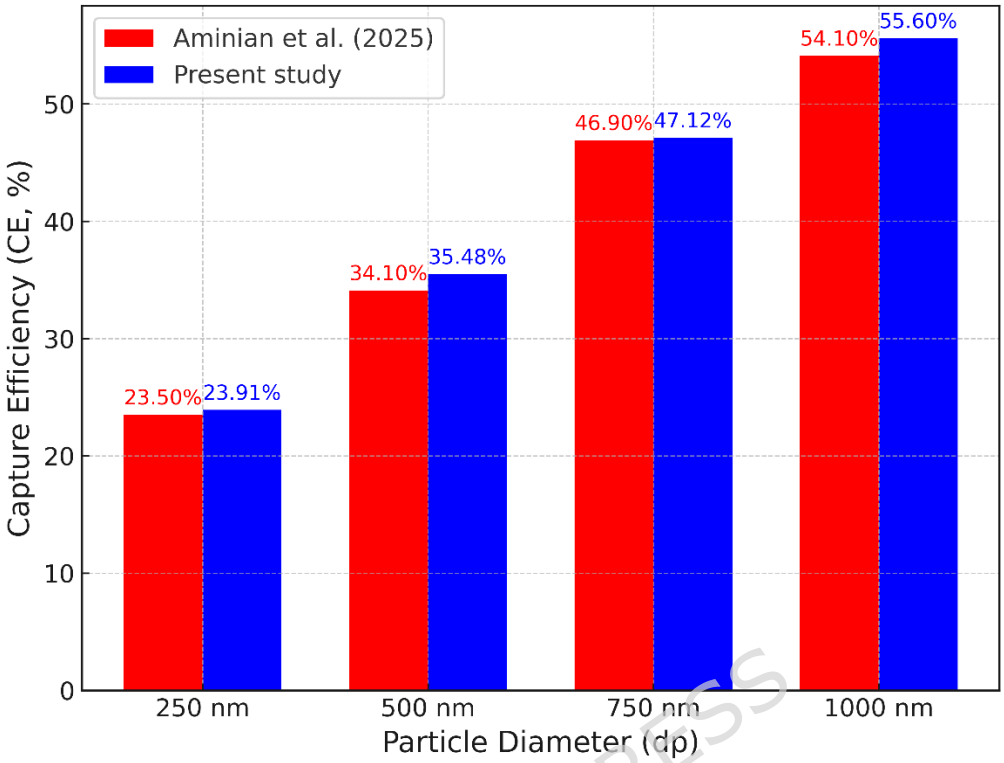

Fig. 4. Validation of results.

The findings confirm that the numerical framework can accurately reproduce results across a diverse range of particle diameters. The close correlation between the current study and the results offset by Aminian, et al. [27], illustrates the strength of the computational approach, particularly nanoparticle transport and CE in arterial flow. Differences may have occurred due to boundary condition assumptions or omitted fluid dynamics or numerical simplifications. Nonetheless, the differences remained below a tolerable error margin (< 2%), which reinforces the validity and accuracy of the method proposed in this paper.

Experimental validation was performed using the benchmark data of [34]. Since experimental MDT data for the human aorta are not available in the literature, the validation was conducted by replicating the same geometry and operating parameters used in their study. Following Takeda et al., the vessel diameter, mean fluid velocity, and nanoparticle diameter were set to 2 mm, 20 cm/s, and 2 μm, respectively. Under these matched conditions, the present numerical model predicted a capture efficiency of 64%, compared with an experimentally measured accumulation of approximately 70% reported by Takeda et al. This difference is attributable to experimental uncertainties in the UV-based concentration measurements and to differences between the idealized magnetostatic and wall conditions in the numerical model and the physical setup (e.g., particle aggregation and surface adhesion effects that are not explicitly modeled). Given these factors, the close agreement in capture efficiency is considered acceptable and supports the validity of the CFD–particle-tracking framework used in this study.

To determine mesh independence study, five grids were used (i.e., G_1=1,021,392, G_2=219,837, G_3=439,264, G_4=865,545, and G_5=1,724,910. The maximum velocity of aorta for the Carreau model of an older patient corresponding to these grid sizes 0.12, 0.138, 0.149, 0.158, 0.160 m/s,

respectively. In terms of gradual refinement of the mesh, significant changes in the velocity profile were observed with the transition from grid G_1 to G_4; however, only a smaller change in the velocity value (0.002 m/s) was observed between G_4 and grid G_5, which was approximately 1% variation in velocity as compared to that predicted by G_4. After this, no further refinement will offer any meaningful differences in the velocity peak or velocity profile. Thus, the G_4 grid with 865,545 elements was fine enough to represent the hemodynamics and was subsequently used for all future simulations. Therefore, it can be concluded that the results generated numerically are mesh independent within an acceptable range.

3.2. Blood phase

In order to achieve the physiological realism required for our experiment, we used the same rheological coefficients obtained from the literature as those provided by [25], [27], and [29] based on their characterization of whole human blood in the shear rate ranges seen in the large arteries. Although there have been reports of a mild increase in plasma viscosity with age, the effect on the high shear region of the thoracic aorta is very low, as viscosity reaches its Newtonian plateau and has an increasingly weak dependence on hematocrit. Our analysis of shear rates ranging between 40 and 300 s^{-1} within the thoracic aorta, for both young and old patients, confirms that the models used in this study predominantly operate in this high shear region. Thus, for the purposes of this study, we utilized the same rheological parameter set for both patient populations, with the intention of only

examining the effects of geometry and hemodynamics on magnetophoretic capture. By doing so, we eliminated any potential confounding effects that would arise from the differences in low-shear microvascular viscosity that may exist between the two populations.

3.2.1. Blood velocity

The blood flow velocity profiles for both the young and old patient models (using the Carreau non-Newtonian viscosity model) are depicted in Fig. 5, at t = 1 s and t = 2 s. The young patient is characterized by a pronounced and centralized jet profile that can be observed, with instantaneous velocities on the order of 1.0 m/s, that smoothly dissipates into the descending thoracic region of the aorta. The shear-thinning characteristics incorporated in the Carreau model to describe non-Newtonian (viscous) behavior allows for velocities to be retained at a specific cross-section where higher shear rates can be maintained while resulting in flow that is streamlined and laminar overall. The old patient has significantly lower absolute velocities, with the maximum peak value not exceeding 0.16 m/s. The velocity contours indicate significant flow perturbations with relative heterogeneity including secondary flow and recirculation within the aortic arch region characterized by relatively large cross-sectional areas, tortuous geometries, and decreased vessel compliance compared to the younger population.

At time t = 2 seconds, which marks the systolic deceleration phase, the young patient continues to demonstrate elevated velocities along the descending

thoracic aorta, while the old patient continues to show stepwise attenuation of flow with maximum velocities at approximately 0.14 m/s. The young aorta continues to show a coherent, stable velocity jet while the old aorta is dominated by fragmented flow structures and localized high-shear regions (near branching and the inner curvature of the arch). These observations underscore that morphology due to age plays a decisive role in altering hemodynamics: younger geometries induce efficient, laminar flow while older geometries promote disturbed, low-shear regions that could promote pathological states such as atherosclerosis. The comparison indicates that the Carreau model provides reasonable and clinically relevant shear-dependent viscosity effects and differentiates the velocity field between young and old.

The current study's findings, which illustrate significantly increased blood velocities in the young patient relative to the old patient, align with the results of Van Ooij, et al. [35] who found that vascular aging corresponds with a significant decrease in aortic flow velocity and wall shear stress due to arterial stiffening and luminal dilation.

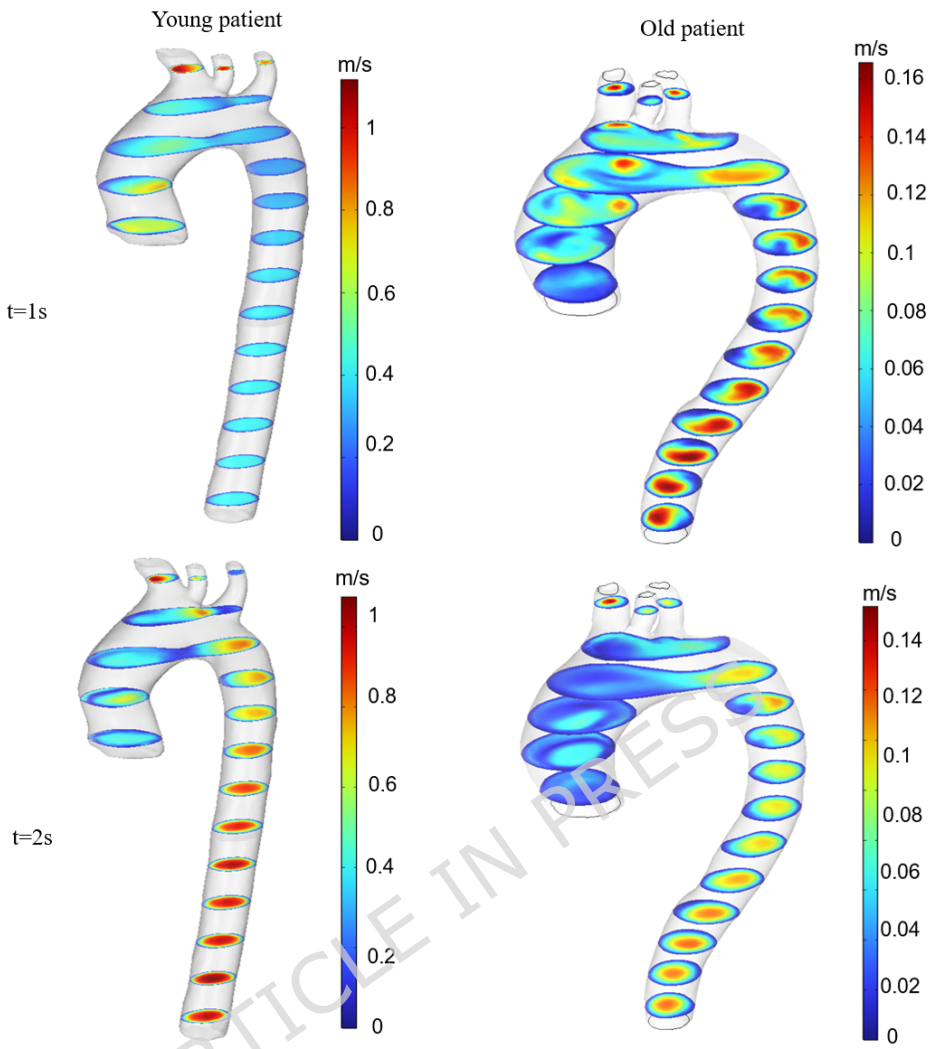

Fig. 5. Blood velocity conturs for both patients at t=1s, and t=2s.

3.2.2. Blood pressure

The pressure distribution within the aorta for both the young and old patients at t = 1 s and t = 2 s is illustrated in Fig. 6. At t = 1 s, which corresponds to the systolic upstroke, the young patient demonstrates distinctly increased peak pressures, measuring greater than 1400 Pa in the ascending aorta and arch. The pressure gradient is well defined along the length of the vessel, reflecting high pressures found proximally, and diminishing as the direction

moves toward the descending thoracic connection. In contrast, the old patient experiences higher pressures of approximately 1100 Pa.

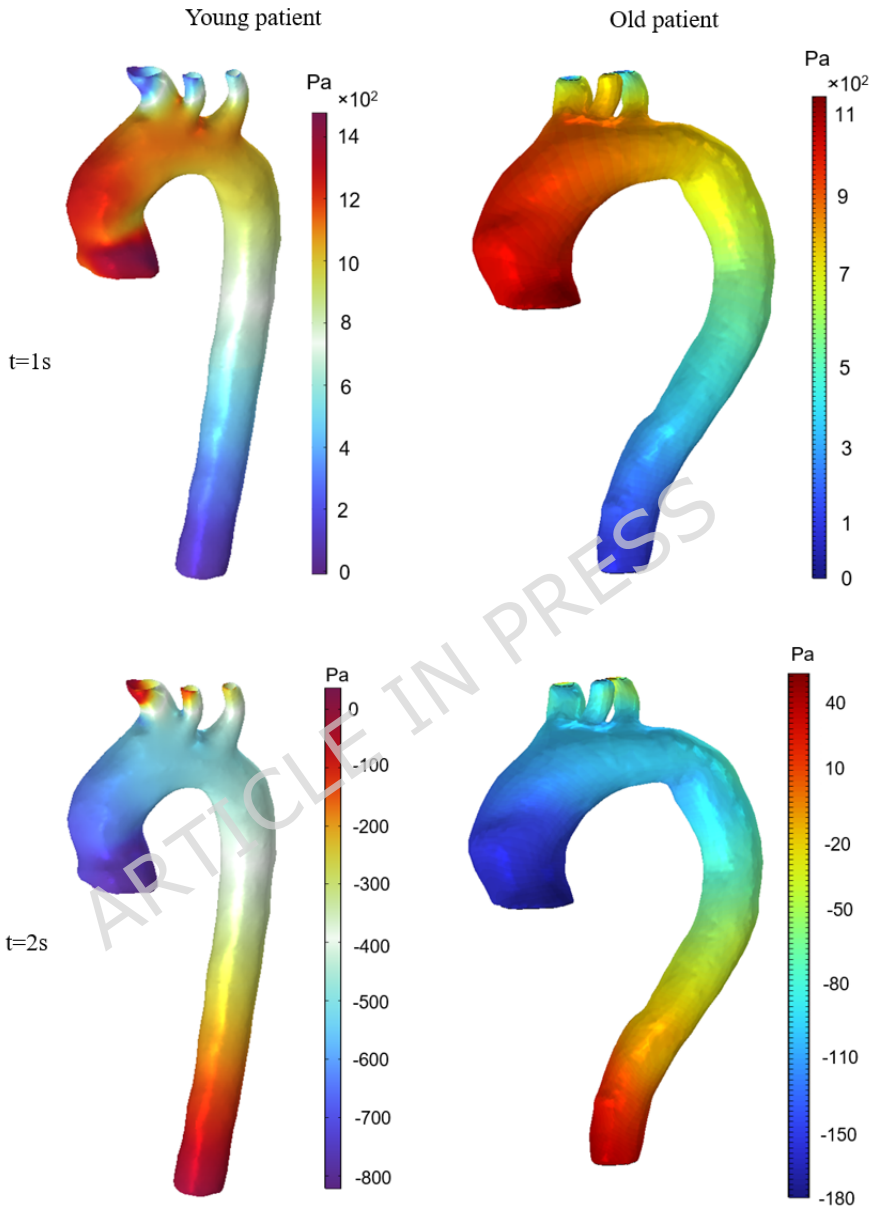

Fig. 6. Blood Pressure conturs for both patients at t=1s, and t=2s.

The pressure field is more uniform, likely due to decreased magnitude of velocity and lower ejection forces present during systolic acceleration as

compared to the young patient. Thus, it seems that the younger aorta, showing a smaller lumen but greater compliance, generates a higher intraluminal pressure as compared to the aged aorta during systolic acceleration. The results from pressure contour analysis (Fig. 6) indicate that the young patient showed higher peak aortic pressures (up to ~1400 Pa) than the old patient (~1100 Pa), with age being associated with a more muted pressure distribution across the aortic arch. These findings are also in agreement with the modeling-focused study of Pagoulatou and Stergiopulos [36], which demonstrated that, due to a stiffening of the proximal aorta during aging, the forward pressure wave was augmented resulting in higher systolic and pulse pressures in younger subjects, while amplification was reduced in older subjects. The agreement between our 3D patient-specific simulations and the large-scale modeling studies provides solid validation that aortic stiffening and wave dynamics drive the age-related decrease in central pressure seen in older patients.

At the 2 second mark, signifying the deceleration phase, the pressure in both patients begins to shift towards lower values. The young patient experiences a dramatic drop in pressure in the descending thoracic aorta with minimum pressures approaching –800 Pa, while the old patient has a smaller drop with minimum pressures of approximately –180 Pa. The decrease in pressure for the young patient exhibits greater values due to the August velocity reading and smaller vessel cross-sectional area facilitating facilitated flow acceleration and subsequent pressure reduction. Conversely, the dilated

lumen of the old patient suppresses pressure wave variation, leading to a smaller peak-to-trough pressure variation. Ultimately, these results point to an important age related dependence of the arterial hemodynamics on morphology: younger vessels will be subjected to relatively higher peak pressures and sharper pressure gradients in contrast to older geometry which will exhibit a dampened pulsatile behavior. Given that the amplitude of aortic pressure decreases with aging, this will inevitably alter hemodynamic loading of the arterial wall, as well as diminished efficiency in the perfusion process and particle transport, see Fig. 6.

The aortic models of elderly and young patients are presented in Table 2 in terms of key haemodynamic characteristics. In terms of haemodynamic properties, the most significant difference between the young model and the elderly model is peak systolic velocity; the young aorta had a maximum peak systolic velocity of 1.10 m/s compared to the 0.16-m/s maximum peak systolic velocity of the elderly patient. This difference is attributable to the smaller luminal area of the young aorta compared to that of the elderly patient, as well as the increased strength of the ventricular ejection associated with the younger physiology. The maximum pressure measured in the young aorta was also significantly higher (1.42 kPa) than the maximum pressure measured in the elderly aorta (1.10 kPa), which reflects the higher acceleration of flow in the young model. Conversely, the elderly aorta exhibited significantly lower wall shear stress than the young aorta; the peak wall shear stress measured in the elderly aorta was 1 Pa compared to the 3.8 Pa peak wall shear stress

measured in the young aorta. This difference is consistent with the age-related increase in vessel diameter and the decrease in flow velocity associated with increased age, which together reduce the amount of shear force exerted on the vessel wall.

Table 2. Quantitative comparison of maximum velocity, pressure, and wall shear stress in young and old aortic models.

Parameter	Young patient	Old patient
Max velocity (m/s)	1.10	0.16
Max pressure (kPa)	1.42	1.10
Max WSS (Pa)	3.8	1

3.3. Magnetic field

In Figure 7, the spatial distribution of the magnetic flux density generated by the cylindrical permanent magnet is illustrated. The magnetic field intensity is approximately 1.4 T at its peak value in the aortic domain, with decreasing field strength as distance increases from the location of the magnet. Notably, the highest value of magnetic intensity is located in the area of interest (ROI) within the descending thoracic aorta, the specific area targeted by the magnetic force for capturing nanoparticles.

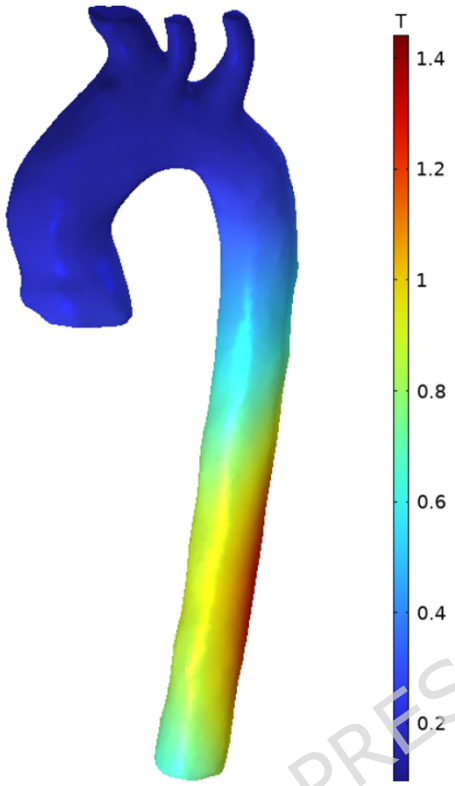

Fig. 7. Magnetic field intensity contur produced by a cylindrical permanent magnet.

This means that this external magnetic field will provide the strongest magnetic force in the location for which retention of the particles is desirable, thereby maximizing targeting efficacy. Because the same external magnetic field was applied to young and old patient-specific geometries, we have only present one case to avoid redundancy.

The magnetic field strength that has been applied is within a range that is deemed safe for human exposure in the clinical environment, as this level of 2 T or lower is well accepted as being safe for diagnostic imaging and even therapeutic applications, (ICNIRP, FDA). Thus, patient safety is assured while

maintaining adequate strength and gradient to facilitate nanoparticle dynamics. The overlap assessing the maximum (or closely maximum) magnetic flux density of the area, as well as the region of interest (ROI), supports enhanced nanoparticle deposition, indicating the field parameters have an acceptable level of physiologic safety, and consideration of the maximum flux density makes it optimal for magnetically targeting nanomedicine.

3.4. Capture efficiency

In this section, the effect of magnetic field intensity, particles' diameter, and non-Newtonian aspect of blood on the nanoparticles' CE for both young and old patients is investigated. The results for each case are presented and compared, then the efficiency of the MDT in that patient is discussed.

3.4.1. Non-Newtonian models

The influence of the Non-Newtonian characteristics on nanoparticles' capture efficiency was investigated. Fig. 8 plots the capture efficiency of the nanoparticle as a function of the particle size for the different blood rheology models (Newtonian, Carreau, Power Law, and Casson-Papanastasiou) for the older patient under a magnetic flux density of 1.5 T. It is observed that the capture efficiency for all models increased monotonically with increasing particle size, as the magnetic force began to dominate over the hydrodynamic drag as particle diameter increased. Larger nanoparticles produced greater magnetic forces ($F_m \propto V_p \cdot \nabla B$), which increased the likelihood of being

deflected away from the bloodstream and captured in the target region, and this statement is in agreement with previous magnetophoretic studies where larger particles had higher relative retention due to size-dependent susceptibility [37].

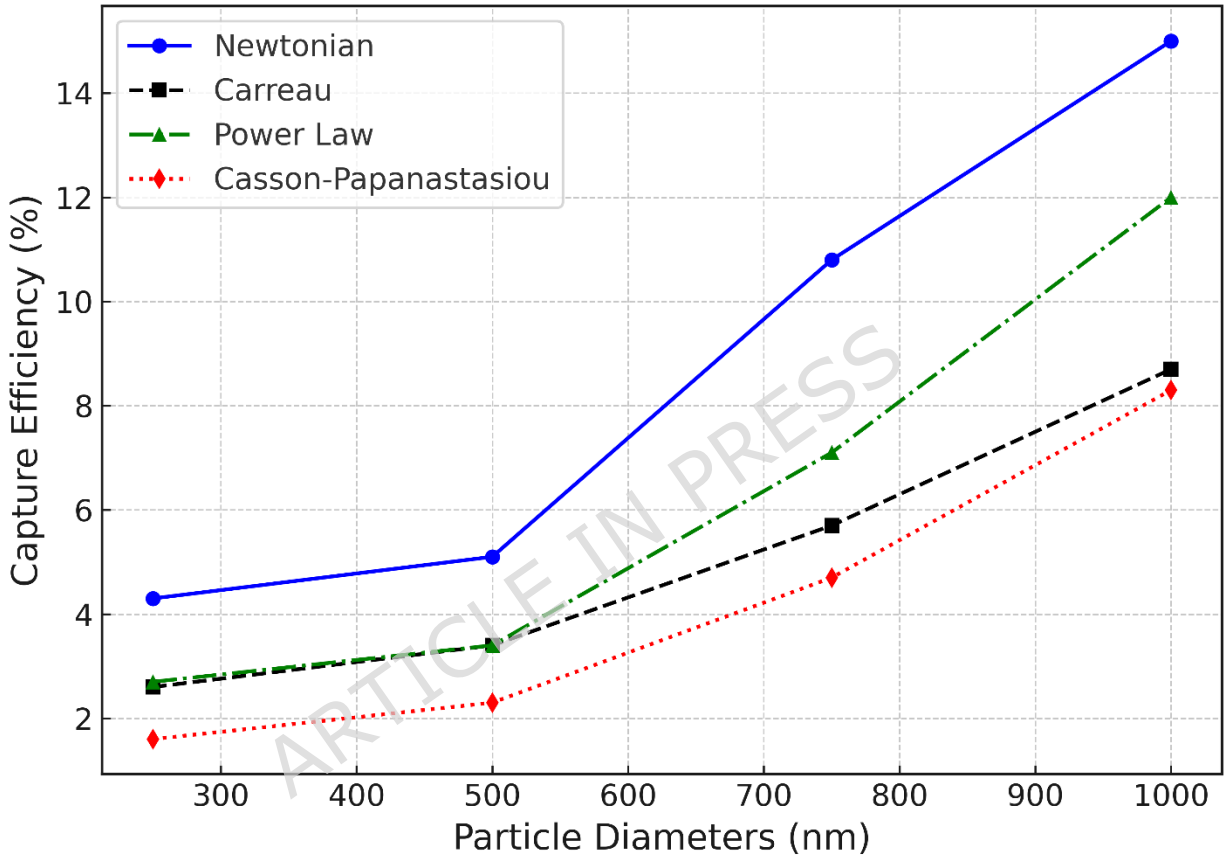

Fig. 8. Nanoparticles' CE for different non-Newtonian models for old patient at B=1.5T.

The Newtonian model consistently yields the highest CE across all particle size ranges, for example, a CE of approximately 15% for 1000 nm particles. The reason for this over-prediction is that Newtonian models tend to ignore the shear-thinning properties of blood and also underestimate viscous

resistance in microvascular flow. Non-Newtonian models have systematically lower efficiencies; for example, the Casson-Papanastasiou generates the lowest CE of 8.3% for 1000 nm particles. The lower CE in these cases is a consequence of the shear-thinning effect which keeps blood viscosity low at high shear rates near the vessel walls allowing for more rapid convective washout of nanoparticles and less time for magnetic capture. Among the non-Newtonian models, the Power Law predicts a higher CE than the Carreau and Casson-Papanastasiou models; this is possibly due to the Power Law being more strongly influential over intermediate shear rates and facilitating a higher caudal nanoparticle deflection towards the vessel wall [38,39].

Fig. 9 illustrates the CE for the paediatric patient as a function of particle diameter at a magnetic flux density of 1.5 T, plotted for four blood rheology models (Newtonian, Carreau, Power law, and Casson-Papanastasiou). As expected, CE increases with the size of the particles in all four models consistent with the scaling of magnetic force using particle volume. Larger induced magnetization particles are more attracted magnetically than resisted by hydrodynamic drag, therefore they are much more apt to deviate from the bloodstream and aggregate into the region of interest.

The Newtonian approximation consistently provided the highest CE among the models, with negligible CE at particle size of 1000 nm when extrapolated at or above, 11%. This overestimation arises from the inability to account for shear-thinning behavior, underestimating viscous losses that occur during blood flow. However, the Carreau, Power Law, and Casson-Papanastasiou

models considered shear-dependent viscosity, resulting in lower efficiencies compared to the Newtonian approach. The Carreau exhibited an intermediate profile, as the CE reached approximately (~) 8.7% at 1000 nm, while the Power Law displayed a stronger growing profile to achieve approximately (~) 9.7%. The lowest efficiencies were predicted by the Casson-Papanastasiou model, particularly for the smaller nanoparticles with only a limited increase to approximately (~) 7.5% at 1000 nm. The differences provoked by the models demonstrate that rheology assumptions can result in substantial differences in nanoparticle transport predictions [40,41].

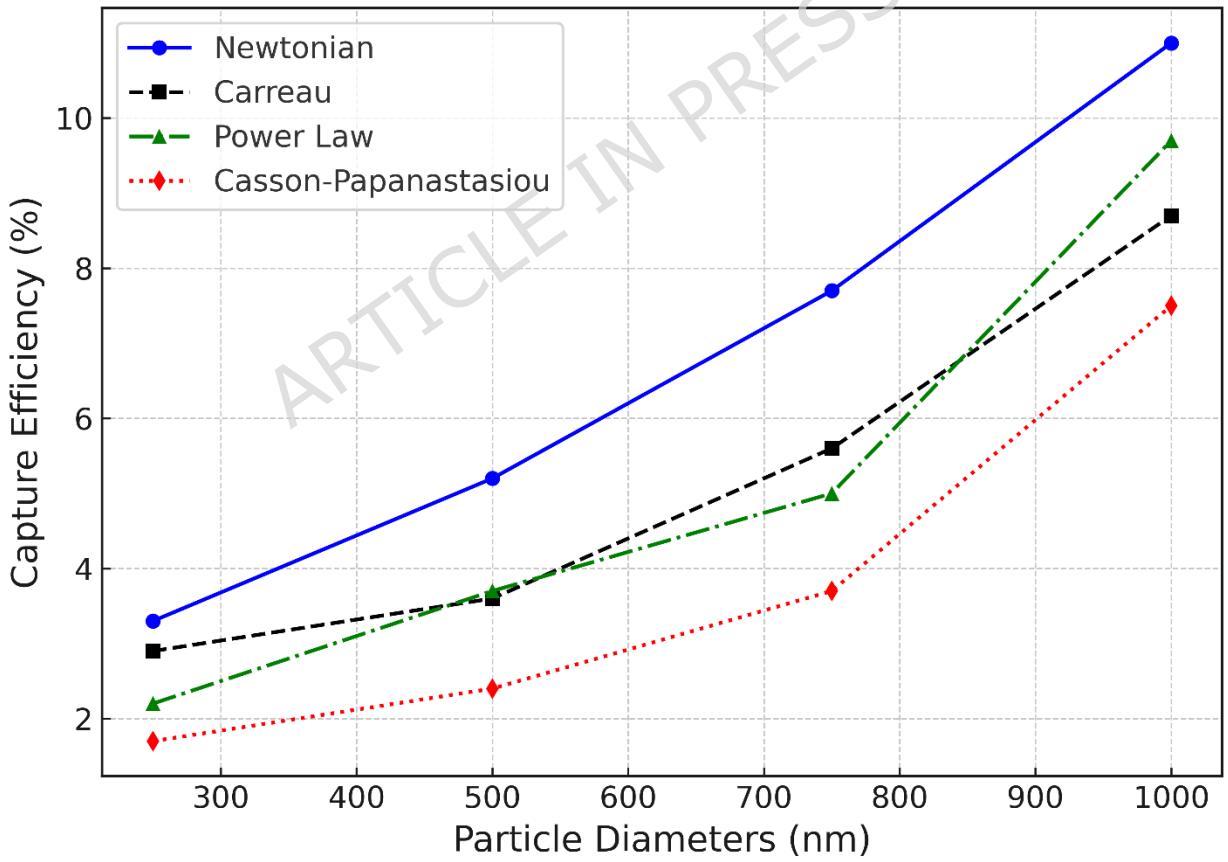

Fig. 9. Nanoparticles' CE for different non-Newtonian models for young patient at B=1.5T.

In the case of the younger patient, the smaller artery diameter, higher baseline shear rates, and uniform velocity distributions lead to a greater retention of nanoparticles, as compared to the older patient scenario. The higher shear rates observed in younger patients further amplify the shear-thinning effect, altering the near-wall velocity profile to create conditions that favor particle margination towards the walls of the vessel. Thus, although Newtonian models will tend to overpredict CE, even the non-Newtonian predictions remain relatively high, more so than aged vessels, demonstrating the additional influence of patient-specific hemodynamics. In summary, these outcomes highlight that both nanoparticle sizes and realistic non-Newtonian models of blood are necessary components for accurate predictions of magnetic drug targeting efficacy in younger vascular systems.

3.4.2. Magnetic field intensity

The influence of the intensity of the magnetic field on the retention of the magnetic nanocarriers is evaluated. Fig. 10 depicts the magnetic particle retention of nanoparticles (dp = 1000 nm, Carreau viscosity) in relation to the magnetic flux density (B) for both young and old subjects. It was found that across all magnetic field intensities investigated, the retention was monotonically increased, verifying the importance of magnetic forces promoting nanocarrier retention. CE values at the lowest intensity of 0.5 T

are 2.1% for the young and 2.4% for the old subject indicating that magnetic force is insufficient to overcoming the high drag forces associated with circulation and the pulsatile shear stress on the surface of the vessels. When the magnetic field was increased to 1.25 T and 1.5 T CE increased to values of 7.25% and 8.7% for the old subject and 6.6% and 8.7% for the young subject. This non-linear increase in retention matches the quadratic function of the magnetic forces and aligned magnetic field gradient traveling along the vessels.

A definitive physiological pattern is observed when contrasting young and older patient geometries. At low magnetic field intensities, the older patient exhibited consistently marginally higher CE values compared to the younger patient, yielding evidence of structural remodeling along with increased vessel diameter seen in the aged aorta leading to slower blood flow velocity and wall shear stress. A decrease in the hemodynamic resistance allows the applied magnetic force to capture and retain the nanoparticles more effectively in the ROI.

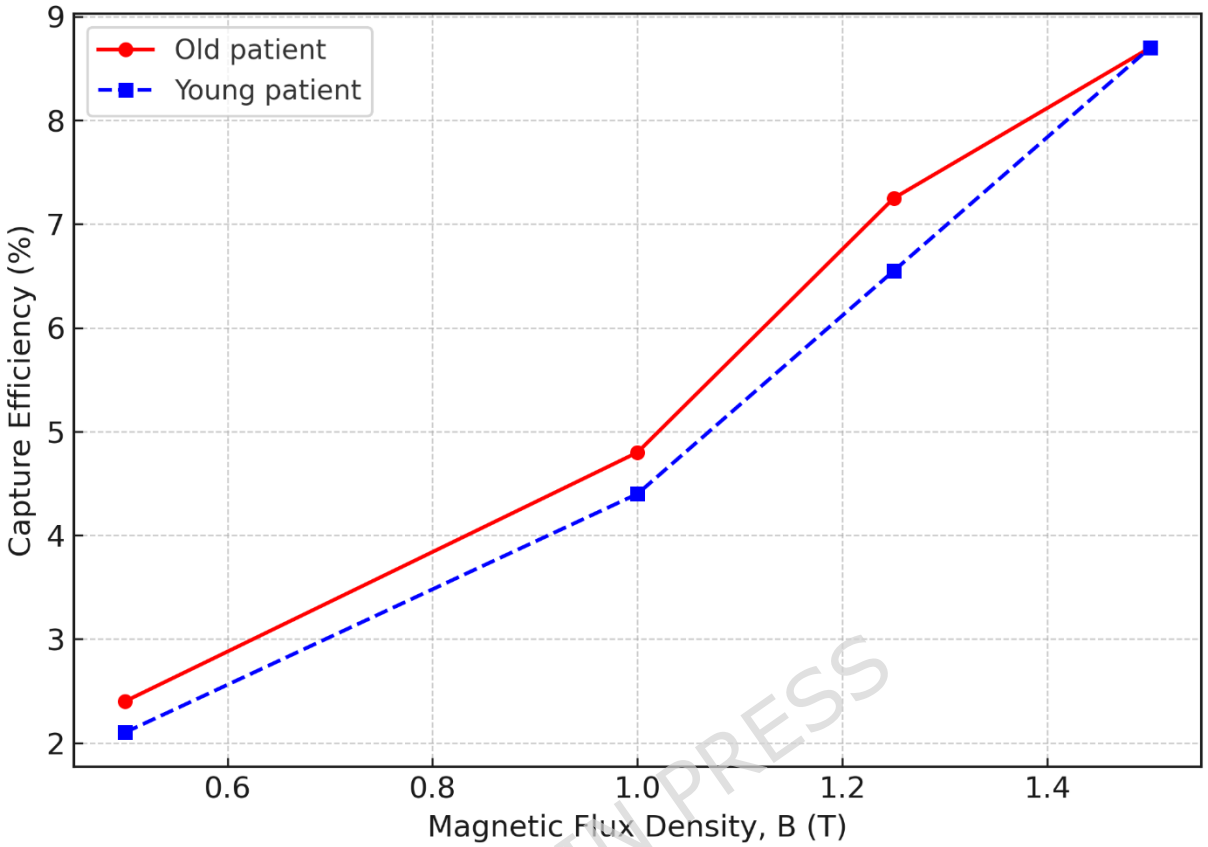

Fig. 10. Nanoparticles' CE for in terms of magnetic field intensity for old and young patients.

On the other hand, the young patient has higher systolic velocities through the aortic arch owing to the steeper curvature of the arch creating stronger inertial forces that work against the magnetic capture of the nanoparticles ultimately making it less efficient at the mid-strength range experiences. There is a noted convergence of the CE values to 8.7% at the maximum intensity of 1.5 T in both cases, indicating that once the applied magnetic force exceeds the hemodynamic stresses, the anatomical variances between the older and young patient may become less rigid in contributing towards

capturing particles. The reported capture efficiencies (maximum ~8.7% at 1.5 T) are consistent with previously reported MDT studies involving extracorporeal or near-body magnets. Larger particles in the 500–1000 nm range experience stronger magnetic forces due to the cubic scaling with particle diameter, enabling partial retention even in high-flow vessels such as the aorta. Prior work has shown <5% CE for sub-200 nm particles [42] and >20% CE for micron-scale particles in stenotic vessels [17]. The present results fall between these regimes and reflect both the achievable magnetic field distribution and the realistic hemodynamics of the descending thoracic aorta. Thus, the CE values reported here represent feasible upper-bound estimates for external MDT systems using clinically realizable permanent magnets.

The CE obtained in this study was evaluated relative to CE values obtained from previous MDT simulations to determine if they represent realistic expectations. Lunnoo and Puangmali [42] reported capture efficiencies less than 5% for 10-200 nm carriers in an arterial section with an implanted magnet having a local field strength of approximately 0.5 T and a gradient of 1.8 T/cm. This demonstrates the challenges associated with maintaining nanoscale particles in high-velocity arterial flow. In contrast, Ardalan et al. [17] demonstrated capture efficiencies of ~21-24% in a stenosed cylindrical vessel in the vicinity of the area of interest where a current-carrying wire was placed close to the area of interest. In addition to the benefits of local magnetic force and constriction of the vessel, this design also takes

advantage of the flow conditions within the stenosis to provide substantially higher capture efficiencies than produced in other work cited. The maximum capture efficiency achieved in this study was 8.7% under conditions similar to those used for the published literature, and therefore falls within a range between these values. Therefore, it is reasonable to believe that an estimated capture efficiency of 8.7% is reasonable for extracorporeal magnetic targeting of particles, especially for high-blood-flow regions such as the aorta.

From a physical viewpoint, the observed phenomena can be attributed to the balance of forces on the nanoparticles. The hydrodynamic drag force, which is dependent on particle velocity and vessel geometry, and the magnetic force, which is dependent on the magnetic susceptibility of the particles and the applied field. The young patient has higher systolic peaks, which increases drag, and slows the efficiency of capturing particles until a stronger field could be applied with greater efficiency. The old patient, on the other hand, may have lower flow velocities, but has a more disturbed secondary flow structure, which may continue to limit uniform capture at the lower fields. The results serve to highlight the potential importance of adjusting magnetic field intensity according to the hemodynamic conditions for the individual patients, wherein a stronger field may be useful to capture an individual with a higher cardiac output, whilst a weaker field may generate particles capture from lower flow rates in older patients [42-44].

The relationship between the distance of the magnet from the aorta and the CE is shown in Fig. 11. As can be seen from the graph, for all sizes of particles, moving the magnet 1 cm, from a distance of 5 cm to a distance of 4 cm, increased the magnetic flux density through the aorta from approximately 1.0 T to 1.5 T, resulting in a significant increase in the CE. Also as predicted, this change in magnet placement corresponds to a non-linear correlation between particle size, magnetic field strength, and CE (noting the rapid decay of the field strength in every direction from the external NdFeB magnet).

With both young and older patient profiles, the larger the particle size, the greater the CE due to the dominant force acting on the particle being magnetic rather than hydrodynamic drag. For example, as shown in the figure, for the old patient profile, the CE for the 1000 nm particles increased from 4.8% to 8.7% when the magnet was moved 1 cm closer to the aortic wall and for the young patient profile, from 4.4% to 8.7%. For smaller particle sizes, the decrease in CE due to the greater distance between the magnet and aorta was proportionally greater, thus making them more susceptible to being washed out by convective forces during normal physiological flow conditions.

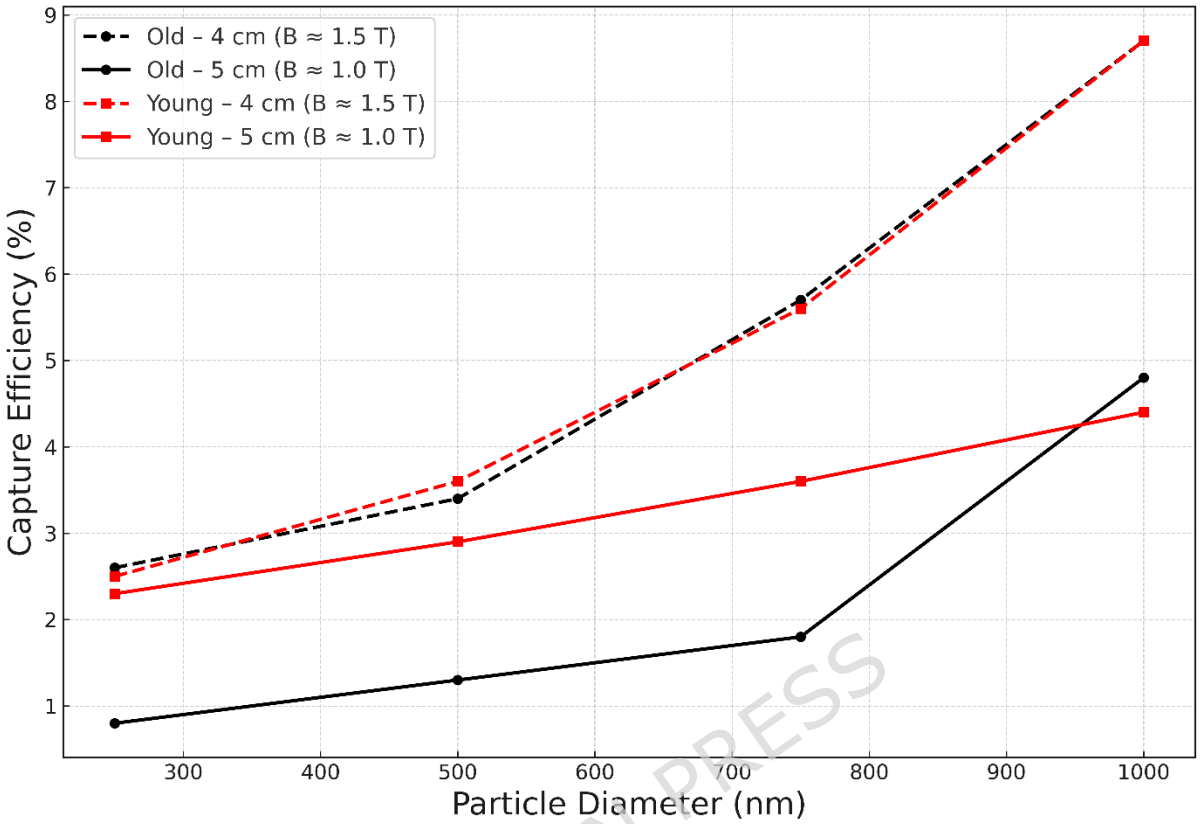

Fig. 11. Effect of magnet-to-aorta distance on nanoparticle capture efficiency in young and old patient-specific aortic flows.

3.4.3. CE in young and old patients

The comparison of CE between young and old patients, as illustrated in Fig. 12, demonstrates a clear modulation of vascular aging on the efficacy of MDT. Across all particle sizes (250–1000 nm) CE were consistently higher in the old patient compared to the young patient, irrespective of the applied rheological model (Carreau or Casson–Papanastasiou). This suggests that the particle transport and deposition processes, when influenced by an external magnetic field, were appreciably impacted by age- related vascular and

hemodynamic changes. One of the primary physiological explanations is related to age-dependent compliance of the vessel and altered flow patterns. Specifically, with advanced age, the aortic lumen enlarges and vascular stiffness increases, resulting in a decrease in wall shear stress and slower bulk velocity. This decrease in velocity may be responsible for an overall less hydrodynamic drag opposing the magnetic force, enabling capture of nanoparticles directly into older patient subjects versus the young patient subjects. Older patients are less pulsatile and experience a slight restriction to the systolic acceleration, which usually provides more inertial forces acting upon nanoparticles, reducing the efficiency of magnetic capture for younger patients. This effect of pulsatility was particularly apparent at larger sizes (750 and 1000 nm) for nanoparticles where it appeared the drag/magnetic force ratio was more favorable in the aged vasculature.

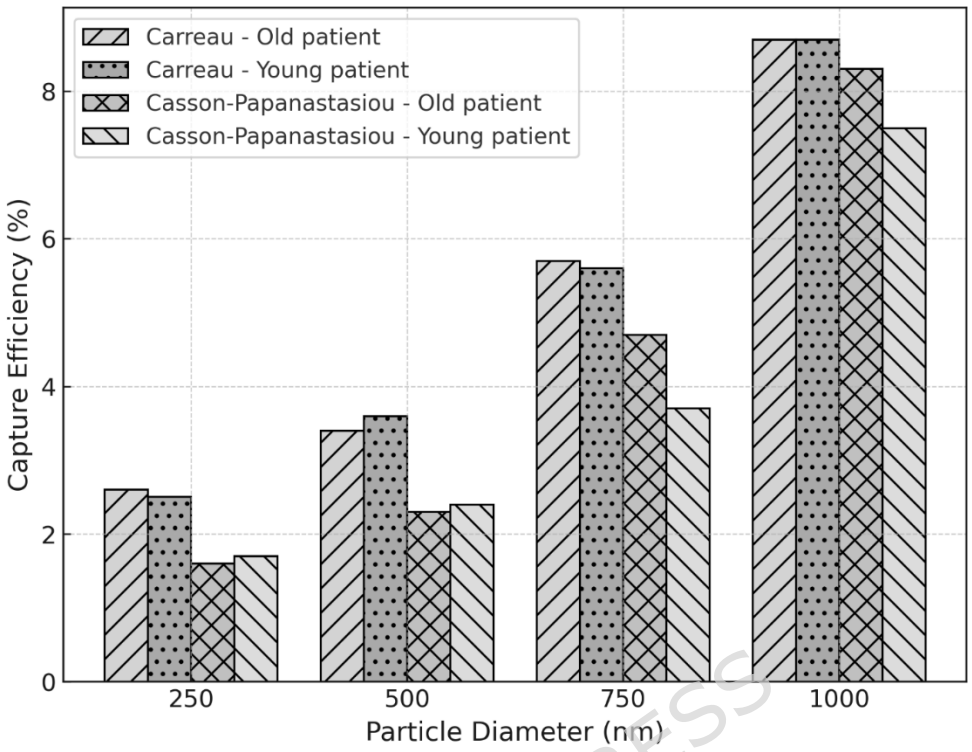

Fig. 12. Nanoparticles' CE for old and young patients.

Moreover, rheological non-Newtonian effects are crucial in altering CE in older populations. The Carreau model reliably predicts more CE than the Casson-Papanastasiou models as it represents the shear-thinning behavior of blood in response to changes in vessel diameter and also from flow pulsatility. In older individuals, shear-thinning induced motion increases particle margination toward the vessel wall, leading to increased capture, whereas young individuals have a larger recovery flow during diastole, redistributing particles more toward the center and preventing accumulation toward the wall. Overall, these data indicate that vascular aging modifies retention of nanoparticles during MDT due to lower hydrodynamic resistance to magnetic attraction, which is a beneficial effect, but must also be considered clinically

as both reduced flow velocities and altered hemodynamics present in the older population can potentially impact drug distribution and perfusion patterns. The older patient model had a higher CE due to a number of different hemodynamic mechanisms working in combination with each other. One of these was that the aorta of an older person to be studied was characterized by having less mean velocity, wall shear stress and pulsatility due to the larger cross-sectional area and increased compliance of the vessel. The former three factors increase the amount of time that particles would spend in the vessel (i.e. longer residence time) as well as lower the amount of resistance to the particles acting under the influence of the magnetic field (i.e. lowering inertial resistance) which allows them to be redirected more effectively towards the vessel wall. Conversely, a younger aorta is devoid of these restrictions thus resulting in a greater mean velocity and strong pulsatile inertia, both of which favor laterally deflected particles thus leading to a reduction in CE. Collectively, the aforementioned geometric and hemodynamic changes yield a common mechanistic explanation for the increase in CE from 1.4-1.6x observed from the older patients compared to their younger counterparts

Magnet placement and patient anatomy must be considered when integrating MDT into clinical practice for treating aortic diseases. The distances between magnets and the ROI, as examined by this investigation (i.e., 4-5cm), align well with the possible extracorporeal magnetic placements around the anterior chest wall for thoracic aorta targets and at/near the abdominal

surface for infrarenal aneurysms. This study supports previous reports on the magnet placements from clinically evaluated magnets based on NdFeB and magnetic targeting systems. The greater accessibility of the thoracic aorta compared to the infrarenal regions for magnetic targeting is primarily a function of their proximity to the chest wall. However, the use of the magnets may be even more advantageous if positioned closer to the abdominal region due to the variability associated with patient body composition.

Elderly patients with aortic dilation or atherosclerotic changes may greatly benefit from using MDT. The increased residence time of the particles in the aorta and diminished flow velocity observed by this investigation enhance magnetophoretic capture of the particles. These findings strongly suggest that combining MDT with other local drug-delivery strategies may be beneficial in patients with age-related aortic disease, including inflammatory lesions, penetrating atherosclerotic ulcers, and early-stage aneurysmal degeneration.

4. Conclusion

This study aimed to compare the efficacy of magnetic drug targeting (MDT) between an older and a younger patient using patient-specific aortic geometries and multiple non-Newtonian blood models. The results demonstrate that the older aortic model exhibited consistently higher CE, approximately 1.4–1.6 times greater than the younger model across all particle diameters and magnetic field strengths. This enhancement is

primarily linked to age-related hemodynamic characteristics: lower mean flow velocities, altered wall shear stresses, and reduced pulsatility increase particle residence time and decrease inertial opposition to magnetic attraction. In contrast, the younger aorta shows higher inertial forces and stronger pulsatile components, both of which diminish magnetic retention and reduce CE. Although increasing the magnetic field strength up to 1.5 T improved CE in both cases, it did not eliminate the difference between age groups, indicating that vascular aging remains a significant determinant of MDT performance. The rheological analysis further suggests that shear-thinning models such as Carreau predict more favorable targeting outcomes than viscoplastic formulations like Casson–Papanastasiou. Overall, these findings indicate that patient age is an important biological and biomechanical variable in MDT, and that optimization of nano-carrier–based therapies should consider age-related differences in vascular geometry and blood rheology to maximize nanoparticle capture.

CRediT authorship contribution statement

Seyed Majid Hosseini: Conceptualization, Methodology, Software, Validation, Formal analysis, Writing – original draft.

Wala Almosawy: Data curation, Visualization, Writing – review & editing; *Rasoul Karimi Takrami:* Methodology, Formal analysis, Investigation, Resources; *Negar Abdi:* Data curation, Validation, Writing – review & editing;

Saman Aminian: Conceptualization, Supervision, Funding acquisition, Project administration, Writing – review & editing.

Declaration of competing interests

The authors declare that they have no known competing financial interests or personal relationships that could have appeared to influence the work reported in this paper.

Funding

Not applicable.

Data Availability statement

The datasets produced and evaluated throughout the present work are available from the corresponding author for reasonable requests. For ethical reasons and patient confidentiality, we cannot share individual-level medical imaging data publicly; thus, it is not available. Notwithstanding, processed simulation data along with the scripts to evaluate and support the findings of this study are available from the authors for reasonable requests.

Etical Statement

This study was entirely computational and did not involve any direct human participation, interventions, or experiments. The patient-specific aortic geometries were reconstructed from retrospective, fully anonymized CT angiography scans, and no identifiable information was used at any stage. According to the Institutional Review Board at the University of Kurdistan,

the use of anonymized retrospective imaging data for computational modeling does not require formal ethics approval or informed consent, and the requirement was waived.

References

1 Buja, L. M., Zhao, B., Vela, D., Segura, A. & Narula, N. Pathobiology of Aortic Aneurysms and Dissections: Synthesis of Recent Investigations and Evolving Insights. *JACC: Advances* **4**, 101682 (2025).

2 Ferrer, M., Altadill, F., Tabilo, J. & Barros, A. Impact of age-related arterial degeneration and inflammation on the presentation and etiopathogenesis of acute aortic syndrome. *European Heart Journal: Acute Cardiovascular Care* **13**, zuae036. 016 (2024).

3 Alcorn, H. G., Wolfson Jr, S. K., Sutton-Tyrrell, K., Kuller, L. H. & O'Leary, D. Risk factors for abdominal aortic aneurysms in older adults enrolled in The Cardiovascular Health Study. *Arteriosclerosis, thrombosis, and vascular biology* **16**, 963–970 (1996).

4 Maleszewski, J. J. Inflammatory ascending aortic disease: perspectives from pathology. *The Journal of thoracic and cardiovascular surgery* **149**, S176–S183 (2015).

5 Czerny, M. *et al.* Current options and recommendations for the use of thoracic endovascular aortic repair in acute and chronic thoracic aortic disease: an expert consensus document of the European Society for Cardiology (ESC) Working Group of Cardiovascular Surgery, the ESC Working Group on Aorta and Peripheral Vascular Diseases, the European Association of Percutaneous Cardiovascular Interventions (EAPCI) of the ESC and the European Association for Cardio-Thoracic Surgery (EACTS). *European Journal of Cardio-Thoracic Surgery* **59**, 65–73 (2021).

6 Organization, W. H. World Health Organization Fact Sheets on Cardiovascular Diseases. *World Health Organization, Fact sheet N* **317** (2015).

7 Ferreira, J. P. *et al.* World heart federation roadmap for heart failure. *Global heart* **14**, 197–214 (2019).

8 Le Huu, A. *et al.* Endovascular therapy for patients with heritable thoracic aortic disease. *Annals of Cardiothoracic Surgery* **11**, 31 (2022).

9 Afilalo, J. *et al.* Addition of frailty and disability to cardiac surgery risk scores identifies elderly patients at high risk of mortality or major morbidity. *Circulation: Cardiovascular Quality and Outcomes* **5**, 222–228 (2012).

10 Tu, L. *et al.* Targeted drug delivery systems for atherosclerosis. *Journal of Nanobiotechnology* **23**, 306 (2025).

11 Lübbe, A. S., Alexiou, C. & Bergemann, C. Clinical applications of magnetic drug targeting. *Journal of Surgical Research* **95**, 200–206 (2001).

12 Shirvalilou, S. *et al.* Development of a magnetic nano-graphene oxide carrier for improved glioma-targeted drug delivery and imaging: in vitro and in vivo evaluations. *Chemico-biological interactions* **295**, 97–108 (2018).

13 Xu, Z., Mousavi, T. & Ainslie, M. Numerical simulation of magnetic drug targeting for lung cancer therapy using a bulk superconducting magnet. *Drug Delivery* **32**, 2490836 (2025).

14 Hua, M.-Y. *et al.* Magnetic-nanoparticle-modified paclitaxel for targeted therapy for prostate cancer. *Biomaterials* **31**, 7355–7363 (2010).

15 Issa, B., Qadri, S., Obaidat, I. M., Bowtell, R. W. & Haik, Y. PEG coating reduces NMR relaxivity of Mn0. 5Zn0. 5Gd0. 02Fe1. 98O4 hyperthermia nanoparticles. *Journal of Magnetic Resonance Imaging* **34**, 1192–1198 (2011).

16 Furlani, E. & Ng, K. Analytical model of magnetic nanoparticle transport and capture in the microvasculature. *Physical Review E—Statistical, Nonlinear, and Soft Matter Physics* **73**, 061919 (2006).

17 Ardalan, A., Aminian, S., Seyfaee, A. & Gharehkhani, S. Effects of geometrical parameters on the capture efficiency of nanoparticles under the influence of the magnetic field in a stenosed vessel. *Powder Technology* **380**, 39–46 (2021).

18 Sodagar, H., Sodagar-Abardeh, J., Shakiba, A. & Niazmand, H. Numerical study of drug delivery through the 3D modeling of aortic arch in presence of a magnetic field. *Biomechanics and Modeling in Mechanobiology* **20**, 787–802 (2021).

19 Barnsley, L. C., Carugo, D., Aron, M. & Stride, E. Understanding the dynamics of superparamagnetic particles under the influence of high field gradient arrays. *Physics in Medicine & Biology* **62**, 2333 (2017).

20 Hewlin Jr, R. L. & Tindall, J. M. Computational assessment of magnetic nanoparticle targeting efficiency in a simplified circle of willis arterial model. *International Journal of Molecular Sciences* **24**, 2545 (2023).

21 Hewlin Jr, R. L., Smith, M. & Kizito, J. P. Computational assessment of unsteady flow effects on magnetic nanoparticle targeting efficiency in a magnetic stented carotid bifurcation artery. *Cardiovascular Engineering and Technology* **14**, 694–712 (2023).

22 Alizadeh, A. a. *et al.* Numerical investigation of the injection angle of carrier nanoparticles under the effect of different magnetic fields. *Journal of Magnetism and Magnetic Materials* **578**, 170836 (2023).

23 Jalali, S., Jalali, S. & Barati, E. Pulsatile blood flow simulations of magnetic drug targeting (MDT) for drug particles dispersion through stenosis asymmetric and symmetric vessels. *Journal of Magnetism and Magnetic Materials* **590**, 171649 (2024).

24 Sharma, B. K., Khanduri, U., Kumawat, C. & Duraihem, F. Z. Simulation of Magnetically Targeted Drug Delivery for Two-Phase Blood Flow in

Stenotic Arteries Under Hall and Ion Influence. *Advanced Theory and Simulations*, e00208 (2025).

25 Hussain, M. A., Kar, S. & Puniyani, R. R. Relationship between power law coefficients and major blood constituents affecting the whole blood viscosity. *Journal of Biosciences* **24**, 329–337 (1999).

26 Boyd, J., Buick, J. M. & Green, S. Analysis of the Casson and Carreau-Yasuda non-Newtonian blood models in steady and oscillatory flows using the lattice Boltzmann method. *Physics of Fluids* **19** (2007).

27 Aminian, S., Najafi, M., Saadat, H. & Ashjaee, M. Computational study of halbach-array-driven magnetic targeting for aortic tumor using Non-Newtonian blood flow models. *Computers in Biology and Medicine* **195**, 110580 (2025).

28 Papanastasiou, T. C. Flows of materials with yield. *Journal of rheology* **31**, 385–404 (1987).

29 Könözsy, L. Z. Multiphysics CFD modelling of incompressible flows at low and moderate Reynolds numbers. (2012).

30 Ranjbari, L., Zarei, K., Alizadeh, A. a., Hosseini, O. & Aminian, S. Three-dimensional investigation of capturing particle considering particle-RBCs interaction under the magnetic field produced by an Halbach array. *Journal of Drug Delivery Science and Technology* **79**, 104046 (2023).

31 Tamboli, N. K. & Murallidharan, J. S. Numerical studies on magnetic driven targeted drug delivery in human vasculature. *Journal of the Indian Institute of Science* **104**, 111–145 (2024).

32 Turton, R. & Levenspiel, O. A short note on the drag correlation for spheres. *Powder technology* **47**, 83–86 (1986).

33 Xia, Y. *et al.* Hemodynamic characteristics of dilated ascending aorta in patients with bicuspid aortic valve. *Journal of Cardiothoracic Surgery* **20**, 354 (2025).

34 Takeda, S.-i., Mishima, F., Terazono, B., Izumi, Y. & Nishijima, S. Development of magnetic force-assisted gene transfer system using biopolymer-coated ferromagnetic nanoparticles. *Science and Technology of Advanced Materials* **7**, 308–314 (2006).

35 Van Ooij, P. *et al.* Age-related changes in aortic 3D blood flow velocities and wall shear stress: Implications for the identification of altered hemodynamics in patients with aortic valve disease. *Journal of Magnetic Resonance Imaging* **43**, 1239–1249 (2016).

36 Pagoulatou, S. & Stergiopulos, N. Evolution of aortic pressure during normal ageing: A model-based study. *PLoS One* **12**, e0182173 (2017).

37 Bina, A., Siavashi, M. & Beigzadeh, B. Three-dimensional numerical simulation of magnetic drug delivery in carotid artery with Eulerian-Lagrangian method: Injection point and magnetic field performance analysis. *Journal of Magnetism and Magnetic Materials*, 173164 (2025).

38 Fanelli, C., Kaouri, K., Phillips, T. N., Myers, T. G. & Font, F. Magnetic nanodrug delivery in non-Newtonian blood flows. *Microfluidics and Nanofluidics* **26**, 74 (2022).

39 Yadeta, H. B. & Shaw, S. Unsteady fractional dispersion under controlled targeted drug elimination and non-Newtonian rheology. *Nonlinear Dynamics*, 1–17 (2025).

40 Manshadi, M., Mohammadi, M. & Sanati-Nezhad, A. Investigation of non-Newtonian blood effects on magnetic drug delivery for chemotherapy applications in an artery vessel. *Anal Comput Theor Chem Lett* **1**, 8–14 (2018).

41 Bose, S., Datta, A., Ganguly, R. & Banerjee, M. Implant assisted magnetic drug targetting for non-Newtonian blood flow. (2023).

42 Lunnoo, T. & Puangmali, T. Capture efficiency of biocompatible magnetic nanoparticles in arterial flow: A computer simulation for magnetic drug targeting. *Nanoscale research letters* **10**, 426 (2015).

43 Kenjereš, S. & Righolt, B. Simulations of magnetic capturing of drug carriers in the brain vascular system. *International Journal of Heat and Fluid Flow* **35**, 68–75 (2012).

44 Aryan, H., Beigzadeh, B. & Siavashi, M. Euler-Lagrange numerical simulation of improved magnetic drug delivery in a three-dimensional CT-based carotid artery bifurcation. *Computer Methods and Programs in Biomedicine* **219**, 106778 (2022).